

See discussions, stats, and author profiles for this publication at: <https://www.researchgate.net/publication/231662435>

Inadequacies of the Point–Dipole Approximation for Describing Electron–Nuclear Interactions in Paramagnetic Proteins: Hybrid Density Functional Calculations and the Analysis of NMR...

ARTICLE in THE JOURNAL OF PHYSICAL CHEMISTRY B · AUGUST 1998

Impact Factor: 3.3 · DOI: 10.1021/jp982018q

CITATIONS

25

READS

8

6 AUTHORS, INCLUDING:



Bin Xia

Peking University

135 PUBLICATIONS 2,232 CITATIONS

SEE PROFILE



Brian F Volkman

Medical College of Wisconsin

148 PUBLICATIONS 5,001 CITATIONS

SEE PROFILE



Frank Weinhold

University of Wisconsin–Madison

199 PUBLICATIONS 28,089 CITATIONS

SEE PROFILE



John L. Markley

University of Wisconsin–Madison

576 PUBLICATIONS 18,237 CITATIONS

SEE PROFILE

Inadequacies of the Point-Dipole Approximation for Describing Electron–Nuclear Interactions in Paramagnetic Proteins: Hybrid Density Functional Calculations and the Analysis of NMR Relaxation of High-Spin Iron(III) Rubredoxin

Steven J. Wilkens,[†] Bin Xia,^{†,‡} Brian F. Volkman,[‡] Frank Weinhold,^{†,§} John L. Markley,^{†,‡} and William M. Westler^{*,‡}

National Magnetic Resonance Facility at Madison, Department of Biochemistry, and Department of Chemistry, University of Wisconsin–Madison, 420 Henry Mall, Madison, Wisconsin 53706

Received: April 27, 1998; In Final Form: June 26, 1998

High-level, all-electron, density functional calculations have been used, in conjunction with high-resolution X-ray structural data, to predict, and to compare with experiment, the contribution of unpaired electrons to the relaxation times for ^{15}N nuclei in oxidized *Clostridium pasteurianum* rubredoxin. Published X-ray structures for the iron(III) rubredoxin from *C. pasteurianum* were employed to construct a 104-atom model for the iron center that included all atoms shown to have strong electronic interactions with the unpaired iron electrons. The remainder of the amide nitrogen resonances in the protein, which show no apparent Fermi contact contribution to the chemical shift, are represented in the model by ghost atoms (atoms with no charge or basis functions). This model served as a starting point for quantum mechanical calculations at the B3LYP/6-311G** level, which, in turn, yielded calculated values for eigenvalues of the spin-differential field gradient tensor, which finally yielded expectation values for effective distances between nuclei and the delocalized spin-density. We report here that using effective distances, which are calculated from the spin-differential field gradient tensor, in the Solomon–Bloembergen equation in place of distances measured from the crystal structures greatly improves the correlation for a plot of experimental relaxation rates versus r^{-6} for ^{15}N resonances in *C. pasteurianum* iron(III) rubredoxin. With increases in the speed of computers and algorithms, iterative quantum chemical optimization of paramagnetic center geometries based on NMR-derived distance and angular constraints from paramagnetic interactions should lead to significant improvements in the determination of the structures of paramagnetic centers in proteins by NMR spectroscopy.

Introduction

Rubredoxins are small proteins with the simplest type of an iron–sulfur center: a single iron ion coordinated in an approximately tetrahedral geometry by four cysteine sulfurs. These proteins are strongly paramagnetic in both accessible oxidation states. In the oxidized state, the iron is high-spin ferric ($S = 5/2$), and upon reduction, the iron accepts one electron and becomes high-spin ferrous ($S = 2$). The exact physiological function of most rubredoxins is unknown; however, the rubredoxin from *Pseudomonas oleovorans* has been found to be involved in the hydroxylation of alkanes,^{1–3} and that from *Desulfovibrio gigas* plays a physiological role in the formation of ATP in the presence of oxygen.⁴

Rubredoxins have been investigated by a variety of biophysical techniques, such as EPR,⁵ Mössbauer,^{6,7} and MCD.⁸ Several structures of rubredoxins have been determined by X-ray crystallography.^{9–14} Rubredoxin was the first non-heme iron protein studied by NMR spectroscopy,¹⁵ and a number of NMR studies of rubredoxins have been carried out.^{16–26}

The rubredoxin from *Clostridium pasteurianum*, molecular weight 6100,²⁷ is one of the best studied members of this family.

Its crystal structure in the oxidized form has been solved and refined to a 1.1-Å resolution.^{9,10,14} This protein has been expressed in *E. coli*,²⁸ and we have recently developed biosynthetic methods for labeling Rdx uniformly and selectively with stable isotopes for NMR investigations.²² Using these labeled samples, we have assigned ^1H , ^2H , ^{13}C , and ^{15}N signals in both the diamagnetic^{25,26} and paramagnetic spectral regions (Xia, B., et al., to be published elsewhere).²⁹ Large H/D isotope effects are seen for amide nitrogen resonances that are hydrogen-bonded to cysteine sulfur atoms.^{22,24}

The wealth of NMR and other spectroscopic data, the relative simplicity of the paramagnetic center, and the availability of high-resolution crystal structures make the clostridial rubredoxin an excellent model for theoretical studies. We recently reported all-electron hybrid density functional calculations which accurately predict the isotropic hyperfine shifts of ^1H , ^2H , ^{13}C , and ^{15}N resonances in rubredoxin from models derived from published crystal structures.²⁹ In that study, we were also able to correct errors in the positions of hydrogen atoms in one of the available crystal structures. Here we extend that work by determining the experimental electron–nuclear longitudinal relaxation rates of the hyperfine shifted ^{15}N resonances in oxidized rubredoxin and by accurately predicting the electron–nuclear dipole–dipole relaxation rates from the spin-density distribution obtained from the wave function. We show that the point-dipole approximation for the spin-density distribution is grossly inappropriate for nuclei that are close to the metal

* To whom correspondence should be addressed. E-mail: milo@nmrfam.wisc.edu. Fax: (608)-263-1722.

[†] Graduate Program in Biophysics.

[‡] Department of Biochemistry.

[§] Department of Chemistry.

[‡] Current address: The Scripps Research Institute, La Jolla, CA.

center but that the relaxation behavior of such nuclei can be predicted accurately from the quantum mechanical wave function.

The dominant mechanisms for spin–lattice relaxation of nuclei proximal to a paramagnetic center are dipolar interactions between nuclei and unpaired electron spins.^{30,31} In the analysis of nuclear relaxation data in paramagnetic systems, a common simplification is to assume that the unpaired electron spin is localized on the central metal or distributed symmetrically over the atoms of a metal cluster and that the spin-density can be described by a point-dipole(s) at the position(s) of the atom(s). The distance from the point-dipole to the nucleus of interest is used in the Solomon–Bloembergen equations^{32–34} to obtain relaxation times, which can be compared with experimental values. It has been found that some experimental relaxation data cannot be explained by this simple model, owing to delocalization of unpaired spin-density into ligand orbitals.^{35–38} To avoid the point-dipole approximation, an electron spin-density matrix model was developed,³⁵ which accounts for the finite size of the electron distribution, the delocalization of the electron, and the spin polarization. From this theory an estimate of an “effective distance” r_{eff} is obtained that replaces the electron–nuclear distance in the Solomon–Bloembergen equations. This approach was extended subsequently to unrestricted Hartree–Fock ab initio calculations on a series of hexaaquo transition metal complexes.^{36,37}

Hybrid density functional calculations (B3LYP/6-311G**) on a 104-atom model of the iron–sulfur center of *Clostridium pasteurianum* rubredoxin have proven to be reliable in predicting the isotropic hyperfine NMR chemical shifts of ^1H , ^2H , ^{13}C , and ^{15}N nuclei. Correlations of the calculated shifts with experimental shifts are excellent,²⁹ reflecting the high quality of the wave function. Here, we use the same wave function to calculate the spin-differential field gradient tensor for oxidized rubredoxin, which leads to an effective distance r_{eff} for the electron–nuclear dipolar contribution to the relaxation rates for all of the nitrogen nuclei in the protein. These effective distances are compared with the measured distances in the crystal structure and with experimental NMR relaxation data for oxidized rubredoxin.

Theory

The longitudinal relaxation rate R_1 for a nucleus interacting with unpaired electrons with total spin S is given by the Solomon–Bloembergen (SB) equation (SI units):

$$R_1 = \frac{2}{15} \left(\frac{\mu_0}{4\pi} \right)^2 \gamma_N^2 g_e^2 \mu_B^2 S(S+1) \left[\frac{\tau_c}{1 + (\omega_I - \omega_S)^2 \tau_c^2} + \frac{3\tau_c}{1 + \omega_I^2 \tau_c^2} + \frac{6\tau_c}{1 + (\omega_I + \omega_S)^2 \tau_c^2} \right] \quad (1)$$

γ_I is the nuclear gyromagnetic ratio, g_e is the electron g -factor, μ_B is the Bohr magneton, μ_0 is the magnetic permeability of free space, r is the nuclear–electron spin distance, τ_c is the correlation time for the nuclear–electron interaction vector, which is usually dominated by the electron relaxation rates, and ω_I and ω_S are the radial frequencies of the nucleus and the electron, respectively, in a magnetic field B_0 (Tesla). (Standard values for the physical constants can be found at <http://physics.nist.gov/PhysRefData/contents.html>.)

An implicit assumption in the SB equation is that the distribution of the net spin-density is localized entirely at the position(s) of the metal atom(s). With this approximation, the

net spin-density can be represented as a pure magnetic dipole, and the distance between a given nucleus and the spin-density can be represented by a single number. This is a clear oversimplification in systems with experimentally observed hyperfine-shifted resonances arising from the Fermi contact mechanism whereby the spin-density is delocalized into ligand orbitals. As mentioned above, the r^{-6} distance in the SB equation can be replaced with an effective value r_{eff}^{-6} determined from the distribution of the spin-density described by a density matrix.³⁵ This approach was recast for use with nonempirical methods with the introduction of the electric field gradient \hat{q} .^{36,37} The electric field gradient operator (eq 2) has the same angular dependence as the magnetic single dipole operator and its expectation values in tensor form can be calculated from the wave function.³⁹

$$\hat{q}_{\alpha\beta} = (3r_{\alpha}r_{\beta} - \delta_{\alpha\beta}r^2)/r^5 \quad (2)$$

Here α, β are Cartesian indices and $\delta_{\alpha\beta}$ is the Kronecker delta function. The integral of the normalized, spin-only, density matrix D_{st} times the matrix elements of \hat{q} gives the elements of the spin-differential field gradient tensor (SDFGT),

$$\langle q_{\alpha\beta} \rangle_{\text{spin}} = \sum_{st} D_{st} \langle s | \hat{q} | t \rangle \quad (3)$$

This tensor contains the spin-only contributions to the electric field gradient tensor, which yields the expectation value of the spin-only nuclear magnetic dipole operator. The effective reciprocal sixth power distance r_{eff}^{-6} between the delocalized spin-density and the nucleus is obtained from the matrix elements of $\langle q_{\alpha\beta} \rangle_{\text{spin}}$.³⁶

$$r_{\text{eff}}^{-6} = \frac{1}{4!} \left[\frac{1}{3} (\langle q_{xx} \rangle_{\text{spin}} - \langle q_{yy} \rangle_{\text{spin}})^2 + \langle q_{zz} \rangle_{\text{spin}}^2 + \frac{4}{3} (\langle q_{xy} \rangle_{\text{spin}}^2 + \langle q_{xz} \rangle_{\text{spin}}^2 + \langle q_{yz} \rangle_{\text{spin}}^2) \right] \quad (4)$$

Calculations and Experiments

Published X-ray structures for the iron(III) rubredoxin from *Clostridium pasteurianum* were employed to construct a 104-atom model for the iron center that included all atoms shown to have strong electronic interactions with the unpaired iron electrons.²⁹ The model consisted of the iron center and two hexapeptide chains, Cys⁶–Thr⁷–Val⁸–Cys⁹–Gly¹⁰–Tyr¹¹ and Cys³⁹–Pro⁴⁰–Leu⁴¹–Cys⁴²–Gly⁴³–Val⁴⁴, each containing two cysteines ligated to the iron. A PDB file was generated containing the coordinates of the residues of interest plus Thr⁵ and Val³⁸. InsightII (Molecular Simulations) was employed to convert Thr⁷, Val⁸, and Leu⁴¹ into glycine residues and to truncate residues 5 and 38 to formyl groups (by converting their C $^{\alpha}$ atoms to hydrogens) in order to retain a realistic electronic environment for the N-terminus of each peptide chain. The C-terminal residues of each chain, Val⁴⁴ and Tyr¹¹, were truncated to N -methyl groups by converting their C and C $^{\beta}$ atoms to hydrogens. To simplify the model further, the C $^{\beta}$ and C $^{\gamma}$ atoms of Pro⁴⁰ were converted to hydrogens to yield an N -methylglycine residue. The remainder of the amide nitrogen resonances in the protein, which show no apparent contact contribution to the chemical shift, are represented in the model by ghost atoms (atoms with no charge or basis functions). Ghost atoms provide a convenient way to obtain electrostatic properties at arbitrary points in space without significantly increasing the time cost of the calculation. This model served as a starting point for quantum mechanical calculations at the B3LYP/6-311G** level, which, in turn, yielded calculated values for isotropic

electron–nuclear hyperfine couplings²⁹ and eigenvalues of the spin-differential field gradient tensor, which finally yielded expectation values for effective distances between nuclei and the delocalized spin-density.

Computational efficiency was a particular concern with the 104-atom models. For systems of this size, perturbative and multiconfigurational correlation methods are impractical. Therefore, the spin-unrestricted B3LYP⁴⁰ hybrid density functional approach as implemented in Gaussian 94^{39,41} was employed for all calculations, allowing the effects of spin polarization and electron correlation to be included at a reasonable computational cost. Our results support previous conclusions that the B3LYP hybrid density functional approach offers a good combination of accuracy and computational efficiency,⁴² especially when used in combination with the 6-311G** basis set.⁴³ The calculation of the SDFGT was much less costly than the computation of the wave function. The checkpointed wave function from the 104-atom model alone, without ghost atoms, was used as the initial guess for the self-consistent field (SCF) calculation. Convergence was obtained in only a few SCF iterations and the total computation was usually completed in an overnight run.

The SDFGT was obtained from Gaussian 94 by using the keyword PROP=EFG(IOP(6/17=2,6/26=4)). This combination of options triggers the calculation of eq 3 by using the spin-only density matrix. In Gaussian 94, the spin-density matrix is normalized to the number of unpaired electrons (rather than to unity), and so the values obtained from the SDFGT were divided by the number of unpaired electrons.

Longitudinal relaxation measurements of the hyperfine-shifted ¹⁵N resonances were collected on a Bruker DMX-500 NMR spectrometer by direct observation of the ¹⁵N spectrum using the inversion–recovery method⁴⁴ with the 180° pulse replaced by a composite 180° pulse.⁴⁵ The carrier frequency was adjusted to the center of groups of resonances to reduce errors due to off-resonance effects. The intensities of the peaks were fitted to the equation $M_z = M_0 [1 - 2 \exp(-t^*R_1)]$, where M_z is the measured intensity at recovery time t , M_0 is the equilibrium intensity, and R_1 is the relaxation rate.

Diamagnetic ¹⁵N longitudinal relaxation times were measured on a Bruker DMX-500 NMR spectrometer at 10 °C using two-dimensional refocused heteronuclear single quantum correlation methods. All pulse schemes utilized gradients for sensitivity enhancement and selective pulses for water flip-back.⁴⁶ All spectra were acquired with 16 scans per FID, 150* ¹⁵N points, and 512* ¹H points. Spectral widths were 8333.33 Hz in the ¹H dimension and 1666.67 Hz in the ¹⁵N dimension. Relaxation time values were obtained with relaxation delay $T = 10, 50, 100, 250, 500$, and 1000 ms. Duplicate spectra were recorded for $T = 10$ and 250 ms for estimation of peak height uncertainties. All Fourier transformation of NMR data was performed with FELIX95 (Molecular Simulations). Longitudinal relaxation times were obtained from two-parameter Levenberg–Marquardt fits of a single exponential to the two-dimensional peak maxima. The values for the relaxation rates are included in the Supporting Information (Table 1S).

The diamagnetic resonances of the ¹⁵N have been assigned in both oxidation states,^{25,26} and the hyperfine shifted resonances have been assigned by selective ¹⁵N labeling (Xia, B., et al, manuscript to be published elsewhere).

Analysis

The total relaxation rate R^T for nuclei in paramagnetic proteins can be split into the rate due to electron–nuclear dipolar

interaction R^{SB} , which is described by the SB equation, Fermi contact relaxation R^{FC} , Curie spin relaxation R^C , and all remaining rates R^D found in diamagnetic proteins.

$$R_1^T = R_1^{SB} + R_1^{FC} + R_1^C + R_1^D \quad (5)$$

The Curie and Fermi contact contributions to the relaxation rate are generally small³⁰ and can be estimated from the magnetic susceptibility and the hyperfine coupling constant, respectively. For the Tyr¹¹ N nucleus in rubredoxin, which has the largest hyperfine shift, the Curie contribution is ~2.5% and the Fermi contact contribution is ~0.5% of the dipole–dipole rate, and hence both mechanisms were neglected. Equation 5 can then be simplified to

$$R_1^T = R_1^{SB} + R_1^D \quad (6)$$

Thus the SB equation (eq 1) can be cast into the equation:

$$R_1^T = [Kf(\tau_c)S(S+1)]r^{-6} + R_1^D \quad (7)$$

where K is a collection of the physical constants (see eq 1), S is the total spin, and $f(\tau_c)$ is the correlation function for the electron–nuclear interaction vector, which is usually dominated by the relaxation rate of the electrons. A plot of the observed relaxation rates R_1^T versus r^{-6} (eq 7) has an intercept that should be equal to the diamagnetic relaxation rate for the nuclei due to other mechanisms and a slope that can be used to estimate the electron correlation time.

The correlation time is given by

$$\tau_c^{-1} = \tau_e^{-1} + \tau_r^{-1} + \tau_{ex}^{-1} \quad (8)$$

where τ_e is the electron correlation time, τ_r is the molecular rotational correlation time, and τ_{ex} is a correlation time for exchange processes. For electron–nuclear interactions, the correlation time τ_c is usually dominated by τ_e . The correlation time τ_e for the electron has contributions from both the electron longitudinal relaxation rate R_{1e} and the electron transverse relaxation rate R_{2e} , which may not be equal.^{31,47} An electron correlation time obtained from the slope of eq 7 contains an implicit assumption that R_{1e} is equal to R_{2e} . With this caveat in mind, an estimate for the electron correlation time τ_e can be obtained from the slope of eq 7. For τ_c of 4×10^{-10} s, and for $S = 5/2$, $B = 11.74$ T, the theoretical slope is 3.2×10^6 . The values obtained from the plots of experimental data (Table 1) are all close to this value and are in good agreement with literature values for T_{1e} of high-spin Fe(III).³⁰

The intercept obtained from a plot of eq 7, R_1^D , corresponds to the relaxation rate for a nucleus that is an infinite distance away from the iron center and should be equal to the relaxation rate arising from all mechanisms that do not involve the electron spin-density. The experimental relaxation rates for ¹⁵N nuclei that are distal to the iron atom in rubredoxin have an average value of about 2.5 s⁻¹.

Figure 1A is a plot of eq 7 for the relaxation rates of the hyperfine-shifted and diamagnetic nitrogen resonances in Rdx using distances from the 4RXN crystal structure (Table 1). The assignments for the hyperfine resonances²⁹ and the diamagnetic resonances^{25,26} are described elsewhere. The dashed line is the linear regression obtained by including only the relaxation rates for the hyperfine resonances (black circles). The intercept (134 s⁻¹) for the dashed line is nearly 2 orders of magnitude larger than the measured rates for the diamagnetic ¹⁵N resonances. The slope of this line, 1.73×10^6 , corresponds to a τ_e of

TABLE 1: Regression Analysis of ^{15}N Longitudinal Relaxation Rates vs Measured and Effective Distances

structure ^a	R^2	r_{xtal}			R^2	r_{eff}		
		slope/ $10^6 \text{ s}^{-1} \text{ \AA}^{-6}$	$\tau_c^b /$ 10^6 s^{-1}	intercept ^c / s^{-1}		slope/ $10^6 \text{ s}^{-1} \text{ \AA}^{-6}$	$\tau_c^b /$ 10^6 s^{-1}	intercept/ s^{-1}
4RXN-HYP ^d	0.94	1.73	2.2	133.8	0.92	2.92	3.7	31.1
4RXN	0.90	2.30	2.9	26.1	0.97	3.14	4.0	4.7
5RXN	0.90	2.15	2.7	26.7	0.98	2.98	3.8	6.1
1IRO	0.89	2.21	2.8	26.1	0.96	3.00	3.8	9.3
1IRO-OPT ^e	0.89	2.21	2.8	26.1	0.98	3.02	3.8	3.8

^a The models used for the calculations of r_{xtal} and r_{eff} were derived from oxidized *C. pasteurianum* rubredoxin structures deposited at PDB: 4RXN,⁹ 5RXN,¹⁰ 1IRO.¹⁴ ^b Calculated from eq 1 assuming a single correlation time. ^c The average relaxation rate for the diamagnetic resonances in rubredoxin is $\sim 2.5 \text{ s}^{-1}$. This would be the expected value for the intercept. ^d Only the hyperfine-shifted resonances were included in the regression analysis. ^e The NH bond lengths and angles were geometry optimized at a B3LYP/3-21G* level from the original structure 1IRO.²⁹

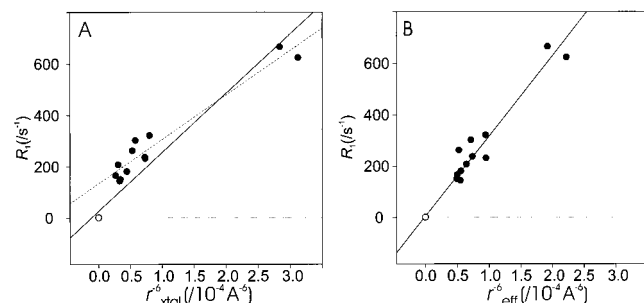


Figure 1. Linear regression fits of relaxation rates of the ^{15}N resonances in oxidized *C. pasteurianum* rubredoxin (in s^{-1}) versus r_{xtal}^{-6} (in \AA^{-6}) measured from the 4RXN crystal structure^{9,10} and r_{eff}^{-6} (in \AA^{-6}) calculated from wave function obtained for the 104-atom model derived from the 4RXN crystal structure by using the SDFGT method described in the text. (A) The dashed line is the linear regression obtained by including only the relaxation rates for the hyperfine shifted resonances (black circles) versus r_{xtal}^{-6} . The solid line shows the same regression analysis for the ^{15}N relaxation rates with inclusion of the diamagnetic nitrogen resonances (open circles). (B) The solid line is the fit obtained from the regression analysis for the relaxation rates of the ^{15}N resonances versus r_{eff}^{-6} (in \AA^{-6}). The parameters of the regression analysis are collected in Table 1.

approximately $2 \times 10^{-10} \text{ s}$, which is not unreasonable for the electron relaxation rate of Fe(III). The R^2 from this regression analysis is 0.94. The results of the regression analysis of this type with input distances r_{xtal} data using different structural models are compared in Table 1.

The solid line in Figure 1A shows the regression analysis for the relaxation data from the hyperfine shifted nitrogen resonances combined with those from the diamagnetic nitrogen resonances (open circles). The intercept (26 s^{-1}) is an order of magnitude larger than the experimental diamagnetic value (Table 1), and the slope (2.3×10^6) corresponds to an electron correlation time of about 2.7×10^{-10} . The resulting R^2 (0.90) is significantly lower than that obtained from the analysis of the hyperfine resonances alone.

Figure 1B is the plot of eq 7 with the distances from the X-ray crystal structures replaced by the effective distances r_{eff} obtained from the eigenvalues of the SDFGT. The line shows the regression analysis for all data points (hyperfine-shifted and diamagnetic nitrogens). The intercept (4.6 s^{-1}) is only about a factor of 2 larger than the average measured diamagnetic rates; the slope is 3.1×10^6 , and the R^2 value (0.97) is better than those obtained with the point-dipole approximation. Results obtained from this type of analysis of data from different structural models derived from X-ray crystallography are listed in Table 1.

Discussion and Conclusion

The Solomon model³² serves well for the description of nuclear–nuclear dipolar relaxation, since the nucleus, to a very

good approximation, can be considered a point-dipole. This equation for $S = 1/2$ and its generalization to $S > 1/2$ ³³ are also commonly used to describe electron–nuclear dipolar relaxation with the assumption, among others,³¹ that all of the electron spin distribution resides at the location of the nucleus that gives rise to the unpaired electrons. In metal clusters it is usually further assumed that the distribution of the electron spin-density is symmetric over the positions of several metal atoms with each acting as a point-dipole. The implicit assumption that there is no delocalization of the spin-density onto the metal ligand atoms is clearly at odds with experimental results that show hyperfine-shifted resonances arising through the Fermi contact mechanism.²⁹ Intuitively, the delocalization of the spin-density onto the metal ligand atoms distributes the spin-density and affects the apparent distance of the nucleus from the unpaired spins.

The SDFGT operator can be evaluated from a suitable quantum mechanical wave function to obtain an effective distance between a nucleus and the delocalized spin-density. We report here that replacing the distance measured from a crystal structure by the effective distance calculated by the SDFGT method greatly improves the correlation for a plot of experimental relaxation rates versus r^{-6} for ^{15}N resonances in *C. pasteurianum* iron(III) rubredoxin. Estimates of the Fermi contact and the Curie spin contributions to relaxation show that these contributions are negligible when compared to the electron–nuclear dipolar relaxation rates. The minor discrepancy between the measured rates of the ^{15}N nuclei that are distal to the iron center and the intercept obtained from the analysis using the effective distances may reflect a small contribution from one of these spin-density-dependent mechanisms to the relaxation of the hyperfine-shifted resonances or possibly from structural differences between the protein in solution and in the crystalline environment.

Figure 2A is a plot of $r_{\text{xtal}} - r_{\text{eff}}$ versus r_{xtal} , where r_{xtal} is the measured distance between individual nitrogen nuclei and the iron atom in the crystal structure and where r_{eff} is the effective distance calculated from the wave function using the SDFGT method. It is intuitive that delocalization would cause some spin-density to be “closer” than the internuclear distance measured in the crystal structure. The majority of the nuclei giving rise to hyperfine-shifted resonances are within 6 \AA of the iron (black circles). For most of these nuclei, the calculated r_{eff} is smaller than r_{xtal} , as intuitively expected (Figure 2B). However, the two cysteine amide nitrogens that are hyperfine shifted to low frequencies have r_{eff} that are larger than the measured distance. This counterintuitive result arises from the location of these nitrogen nuclei in a negative region of the SDFGT. The inset plot (Figure 2B) shows an expansion of the ordinate which suggests a weak positive correlation ($R^2 = 0.82$) for $r_{\text{xtal}} - r_{\text{eff}}$ versus r_{xtal} with a slope of 0.4. These large

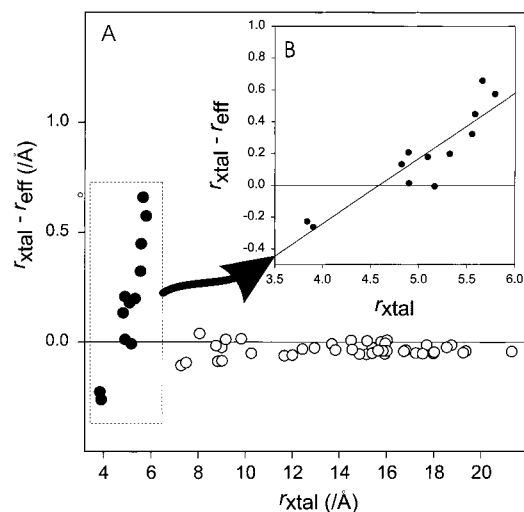


Figure 2. (A) Plot of $r_{\text{xtal}} - r_{\text{eff}}$ versus r_{xtal} , where r_{xtal} is the measured distance between individual nitrogen nuclei and the iron atom in the 4RXN¹⁰ crystal structure and where r_{eff} is the effective distance calculated from the wave function using the SDFGT method (see text). Black circles represent ¹⁵N nuclei that give rise to hyperfine-shifted resonances and open circles represent the “diamagnetic” ¹⁵N nuclei. The horizontal line is drawn at the zero of the abscissa. The inset plot (B) shows an expansion of the ordinate for nuclei that are close to the metal center.

deviations from the uncorrected SB equations document that the point-dipole approximation is wholly unreliable in the extended neighborhood (i.e., $< 7 \text{ \AA}$) of the metal center.

From our calculations in this simple metal center, it appears that metal–nucleus distances determined from the relaxation of the hyperfine-shifted resonances could give constraints with an accuracy of about 1 \AA . The use of relaxation rates to determine distances between a paramagnetic metal center and rapidly relaxing hyperfine-shifted nuclei must be approached with caution. However, given the exquisite geometric sensitivity of the Fermi contact shift²⁹ and the strong dependence of the relaxation rates on the distribution of the spin-density, it might be possible to combine molecular mechanics and/or molecular dynamics with the results of quantum chemical calculations and NMR spectroscopy to obtain high-resolution structures close to the paramagnetic center. Nuclei between 7 and 10 \AA from the metal center (open circles) exhibit only slight differences ($\sim 0.1 \text{ \AA}$) between r_{xtal} and r_{eff} . The paramagnetic contribution to the relaxation rate for these resonances may serve as the basis for crude distance constraints on the position of the metal center. The relaxation rates for nuclei that are greater than about 10 \AA (Figure 2, open circles) away from the metal center are virtually unaffected by the paramagnetic center, and accordingly, the effective distance is nearly equal to the measured distance from the crystal structure.

There is a suggestion of a slight residual bias for the r_{eff} to be somewhat larger than the r_{xtal} for nuclei that are greater than about 10 \AA from the iron atom. This may be an artifact of the calculation, since all of the nitrogen nuclei that do not show hyperfine shifted resonances are represented in the calculation by ghost atoms with no basis functions. The ghost atoms serve only as points in space for the calculation of the SDFGT. Calculations with small models suggest that r_{eff} is overestimated for ghost atoms (data not shown).

The technically challenging experimental determination of the longitudinal relaxation rates for the protons, deuterons, and carbons of the cysteine residues in oxidized rubredoxin have not been reported. However, calculations based on the SDFGT

TABLE 2: Ratios, $R_1^{\text{eff}}/R_1^{\text{xtal}}$, of Predicted Relaxation Rates Obtained from the SDFGT (R_1^{eff}) and Point-Dipole (R_1^{xtal}) Models for Atoms of the Cysteine Ligands

cysteine residue	H ^α	H ^{β2}	H ^{β3}	C ^α	C ^β	C
6	1.10	0.67	0.65	1.41	0.88	1.01
9	0.95	1.05	0.66	1.20	1.62	0.97
39	1.13	0.66	0.66	1.58	0.93	1.06
42	0.96	1.15	0.68	1.34	1.95	1.01

model of the rates for these nuclei show that the point-dipole model would underestimate some relaxation rates by as much as 35% and overestimate others by as much as 58% (Table 2). The point-dipole approximation for the cysteine H^α and C^β atoms show both under- and overestimation for the relaxation rates. The relaxation rates for the H^{β3} atoms for all cysteine residues would be overestimated by the point-dipole approximation, and conversely, the rates for the C^α nuclei would all be underestimated. The patterns of the predicted relaxation rate ratios for proton and carbon nuclei in Cys⁶ and Cys⁹, whose S^γ atoms form hydrogen bonds with the H atoms of the other two cysteine residues, are similar. The ratios are similar for the proton and carbon nuclei in Cys⁹ and Cys⁴², whose S^γ atoms form hydrogen bonds with amino acid residues other than cysteine.

Chae and Markley³⁸ observed in *Anabaena* 7120 heterocyst ferredoxin that the ¹⁵N longitudinal relaxation times are clustered into two sets. Relaxation rates for resonances arising from amide nitrogens greater than 4.2 \AA away from the iron–sulfur cluster in the crystal structure agreed closely with the predicted rates from the point-dipole model, whereas relaxation rates for some amide nitrogen resonances closer to the iron–sulfur center appeared to be farther away from the iron–sulfur center than expected from the point-dipole model. From the results in this paper, we suggest that these nuclei lie in negative regions of the SDGFT and that their effective distances from the paramagnetic center are larger than the distances measured from the crystal structure.

Hybrid density-functional, quantum chemical calculations of metal sites in high-spin iron–sulfur proteins have been shown here to reproduce NMR relaxation rates and, elsewhere, to reproduce Fermi contact shifts²⁹ with high accuracy. There are few experimental NMR relaxation data available that directly demonstrate the inadequacy of the point-dipole approximation. The relaxation data and the calculations presented here are the first direct demonstration of this in a paramagnetic protein. With increases in the speed of computers and algorithms, iterative quantum chemical optimization of paramagnetic center geometries based on NMR-derived distance and angular constraints from paramagnetic interactions should lead to significant improvements in the determination of the structures of paramagnetic centers in proteins by NMR spectroscopy.

Acknowledgment. This work was supported by a grant (GM35976) from the National Institute of General Medical Sciences, National Institutes of Health. Calculations utilized the SGI-Cray Origin 2000 and HP-Convex Exemplar X-Class computers at the National Center for Supercomputing Applications, University of Illinois at Urbana–Champaign, and the Silicon Graphics Onyx at the National Magnetic Resonance Facility at Madison (NMRFAM), which is supported by a grant (RR02307) from the Biomedical Research Technology Program of the National Center for Research Resources, National Institutes of Health. S.J.W. was supported in part by a traineeship from an NIH Molecular Biophysics Training Grant (GM08293).

Supporting Information Available: Table 1S of experimentally measured ^{15}N relaxation rates for oxidized *Clostridium pasteurianum* rubredoxin (1 page). See any current masthead page for ordering information and Internet access instructions.

References and Notes

- (1) Eggink, G.; Lageveen, R. G.; Altenburg, B.; Witholt, B. *J. Biol. Chem.* **1987**, *262*, 17712.
- (2) Eggink, G.; Engel, H.; Vriend, G.; Terpstra, P.; Witholt, B. *J. Mol. Biol.* **1990**, *212*, 135.
- (3) Kok, M.; Oldenhuis, R.; van der Linden, M. P.; Raatjes, P.; Kingma, J.; van Lelyveld, P. H.; Witholt, B. *J. Biol. Chem.* **1989**, *264*, 5435.
- (4) Hurley, J. K.; Salamon, Z.; Meyer, T. E.; Fitch, J. C.; Cusanovich, M. A.; Markley, J. L.; Cheng, H.; Xia, B.; Chae, Y. K.; Medina, M.; Gómez-Moreno, C.; Tollin, G. *Biochemistry* **1993**, *32*, 9346.
- (5) Peisach, J.; Blumberg, W. E.; Lode, E. T.; Coon, M. J. *J. Biol. Chem.* **1971**, *246*, 5877.
- (6) Rao, K. K.; Evans, M. C.; Cammack, R.; Hall, D. O.; Thompson, C. L.; Jackson, P. J.; Johnson, C. E. *Biochem. J.* **1972**, *129*, 1063.
- (7) Schulz, C.; Debrunner, P. G. *J. Phys.—Paris* **1976**, *37*, C6—C6—158.
- (8) Bennett, D. E.; Johnson, M. K. *Biochim. Biophys. Acta* **1987**, *911*, 71.
- (9) Watenpaugh, K. D.; Sieker, L. C.; Jensen, L. H. *J. Mol. Biol.* **1979**, *131*, 509.
- (10) Watenpaugh, K. D.; Sieker, L. C.; Jensen, L. H. *J. Mol. Biol.* **1980**, *138*, 615.
- (11) Frey, M.; Sieker, L. C.; Payan, F.; Haser, R.; Bruschi, M.; Pepe, G.; LeGall, J. *J. Mol. Biol.* **1987**, *197*, 525.
- (12) Stenkamp, R. E.; Sieker, L. C.; Jensen, L. H. *Proteins Struct., Funct. Genet.* **1990**, *8*, 352.
- (13) Adman, E. T.; Sieker, L. C.; Jensen, L. H. *J. Mol. Biol.* **1991**, *217*, 337.
- (14) Dauter, Z.; Wilson, K. S.; Sieker, L. C.; Moulis, J.-M.; Meyer, J. *Proc. Natl. Acad. Sci. U.S.A.* **1996**, *93*, 8836.
- (15) Phillips, W. D.; Poe, M.; Weiher, J. F.; McDonald, C. C.; Lovenberg, W. *Nature* **1970**, *227*, 574.
- (16) Krishnamoorthi, R.; Markley, J. L.; Cusanovich, M. A.; Przysiecki, C. *Biochemistry* **1986**, *25*, 50.
- (17) Werth, M. T.; Kurtz, D. M., Jr.; Moura, I.; LeGall, J. *J. Am. Chem. Soc.* **1987**, *109*, 273.
- (18) Blake, P. R.; Park, J.-B.; Bryant, F. O.; Aono, S.; Magnuson, J. K.; Eccleston, E.; Howard, J. B.; Summers, M. F.; Adams, M. W. *Biochemistry* **1991**, *30*, 10885.
- (19) Blake, P. R.; Lee, B. M.; Summers, M. F.; Adams, M. W.; Park, J.-B.; Zhou, Z. H.; Bax, A. *J. Biomol. NMR* **1992**, *2*, 527.
- (20) Blake, P. R.; Park, J.-B.; Adams, M. W. W.; Summers, M. F. *J. Am. Chem. Soc.* **1992**, *114*, 4931.
- (21) Blake, P. R.; Park, J.-B.; Zhou, Z. H.; Hare, D. R.; Adams, M. W.; Summers, M. F. *Protein Sci.* **1992**, *1*, 1508.
- (22) Xia, B.; Westler, W. M.; Cheng, H.; Meyer, J. P.; Moulis, J.-M.; Markley, J. L. *J. Am. Chem. Soc.* **1995**, *117*, 5347.
- (23) Gaillard, J.; Zhuang-Jackson, H. Y.; Moulis, J.-M. *Eur. J. Biochem.* **1996**, *238*, 346.
- (24) Xia, B.; Wilkens, S. J.; Westler, W. M.; Markley, J. L. *J. Am. Chem. Soc.* **1998**, *120*, 4893.
- (25) Prantner, A. M.; Volkman, B. F.; Wilkens, S. J.; Xia, B.; Markley, J. L. *J. Biomol. NMR* **1997**, *10*, 411.
- (26) Volkman, B. F.; Prantner, A. M.; Wilkens, S. J.; Xia, B.; Markley, J. L. *J. Biomol. NMR* **1997**, *10*, 409.
- (27) Petillot, Y.; Forest, E.; Mathieu, I.; Meyer, J.; Moulis, J.-M. *Biochem. J.* **1993**, *296*, 657.
- (28) Mathieu, I.; Meyer, J.; Moulis, J.-M. *Biochem. J.* **1992**, *285*, 255.
- (29) Wilkens, S. J.; Xia, B.; Weinhold, F.; Markley, J. L.; Westler, W. M. *J. Am. Chem. Soc.* **1998**, *120*, 4806.
- (30) Bertini, I.; Luchinat, C. *NMR of Paramagnetic Molecules in Biological Systems*; Benjamin/Cummings: Menlo Park, CA, 1986.
- (31) Kowalewski, J.; Nordenskiöld, L.; Benetis, N.; Westlund, P.-O. *Prog. Magn. Reson. Spectrosc.* **1985**, *17*, 141.
- (32) Solomon, I. *Phys. Rev.* **1955**, *99*, 559.
- (33) Bloembergen, N. *J. Chem. Phys.* **1957**, *27*, 572.
- (34) Bloembergen, N.; Morgan, L. O. *J. Chem. Phys.* **1961**, *34*, 842.
- (35) Gottlieb, H. P. W.; Barfield, M.; Doddrell, D. M. *J. Chem. Phys.* **1977**, *67*, 3785.
- (36) Kowalewski, J.; Laaksonen, A.; Nordenskiöld, L. *J. Chem. Phys.* **1981**, *74*, 2927.
- (37) Nordenskiöld, L.; Laaksonen, A.; Kowalewski, J. *J. Am. Chem. Soc.* **1982**, *104*, 379.
- (38) Chae, Y. K.; Markley, J. L. *Biochemistry* **1995**, *34*, 188.
- (39) *Gaussian 94 Revision E.2*. Frisch, M. J.; Trucks, G. W.; Schlegel, H. B.; Gill, P. M. W.; Johnson, B. G.; Robb, M. A.; Cheeseman, J. R.; Keith, T.; Petersson, G. A.; Montgomery, J. A.; Raghavachari, K.; Al-Laham, M. A.; Zakrzewski, V. G.; Ortiz, J. V.; Foresman, J. B.; Cioslowski, J.; Stefanov, B. B.; Nanayakkara, A.; Challacombe, M.; Peng, C. Y.; Ayala, P. Y.; Chen, W.; Wong, M. W.; Andres, J. L.; Replogle, E. S.; Gomperts, R.; Martin, R. L.; Fox, D. J.; Binkley, J. S.; Defrees, D. J.; Baker, J.; Stewart, J. P.; Head-Gordon, M.; Gonzalez, C.; Pople, J. A. 1995. Pittsburgh, PA, Gaussian, Inc.
- (40) Becke, A. D. *J. Chem. Phys.* **1993**, *98*, 5648.
- (41) The form of the B3LYP functional implemented in ref 39 is given in: Stephens, P. J.; Devlin, F. J.; Chabalowski, C. F.; Frisch, M. J. *J. Chem. Phys.* **1994**, *98*, 11623.
- (42) Cohen, M. J.; Chong, D. P. *Chem. Phys. Lett.* **1995**, *234*, 405.
- (43) Lim, M. H.; Worthington, S. E.; Dulles, F. J.; Cramer, C. J. *ACS Symp. Ser.* **1996**, *629*, 402.
- (44) Vold, R. L.; Waugh, J. S.; Klein, M. P.; Phelps, D. E. *J. Chem. Phys.* **1968**, *48*, 3831.
- (45) Freeman, R.; Kempersell, S. P.; Levitt, M. H. *J. Magn. Reson.* **1980**, *38*, 453.
- (46) Farrow, N. A.; Muhandiram, R.; Singer, A. U.; Pascal, S. M.; Kay, C. M.; Gish, G.; Shoelson, S. E.; Pawson, T.; Forman-Kay, J. D.; Kay, L. E. *Biochemistry* **1994**, *33*, 5984.
- (47) Reuben, J.; Reed, G. H.; Cohn, M. *J. Chem. Phys.* **1970**, *52*, 1617.